

Article

# Rational Electrolyte Formulation for Sodium Metal Batteries Operating in Extremely Cold Environments

Chuanlong Wang, Peiyu Wang, and Weiyang Li \*

Thayer School of Engineering, Dartmouth College, Hanover, NH 03755, USA; weiyang.li@dartmouth.edu  
Received: 3 March 2026; Revised: 27 March 2026; Accepted: 30 March 2026; Published: 31 March 2026

**Abstract:** Sodium metal batteries have shown considerable potential when operated at ambient temperatures. However, their performance in cold environments is constrained by increased electrolyte resistance with decreasing temperature and dendritic sodium plating associated with unstable solid electrolyte interphase (SEI), which are primarily influenced by the electrolyte composition. In this study, we present an electrolyte formulation that remains thermally stable down to  $-150\text{ }^{\circ}\text{C}$ , which not only facilitates low internal resistance but also contributes to the formation of a protective SEI under cryogenic conditions. When cycled at  $-40\text{ }^{\circ}\text{C}$  at  $1\text{ mA cm}^{-2}$ , the sodium metal electrode exhibits a low overpotential of only 16 mV over 750 h; even at an ultra-low temperature of  $-80\text{ }^{\circ}\text{C}$ , the electrode demonstrates remarkable long-term stability with a low overpotential of 54 mV sustained over 1500 h at  $0.5\text{ mA cm}^{-2}$ . Furthermore, full cell evaluations when pairing with  $\text{Na}_3\text{V}_2(\text{PO}_4)_3$  cathode reveal a high average Coulombic efficiency exceeding 99.1% and a capacity retention over 83% after 100 cycles at both  $-40\text{ }^{\circ}\text{C}$  and  $-80\text{ }^{\circ}\text{C}$ .

**Keywords:** sodium metal battery; low temperature; ether electrolyte; sodium hexafluorophosphate; solid electrolyte interphase

## 1. Introduction

Lithium-ion batteries (LIBs) are widely employed in portable electronics and electric vehicles owing to their high energy and power densities, as well as their prolonged cycle life [1–3]. However, LIBs suffer considerable energy and power losses at low operating temperatures, particularly below  $-20\text{ }^{\circ}\text{C}$  [4,5]. This significantly restricts their applications under cold conditions [5,6], including military and aerospace, polar exploration, cold-chain logistics, and renewable energy storage in cold climates. To overcome the low-temperature operational hurdles, beyond LIB technologies, specifically those utilizing lithium metal anodes are being investigated with promising results [7–16]. Meanwhile, the escalating cost of lithium has compelled the research community to explore alternative energy storage technologies. Sodium (Na) metal emerges as a particularly attractive anode candidate for Na battery chemistry because of its high theoretical specific capacity ( $1166\text{ mAh g}^{-1}$ ), low electrode potential ( $-2.714\text{ V}$  versus the standard hydrogen electrode), and much lower cost and high abundance of Na resources compared to the lithium counterparts [17–22]. Yet, comprehensive understanding of the electrochemical behavior of Na metal anodes under low-temperature conditions remain elusive.

Formulating the appropriate electrolyte composition is critical for enabling the Na metal anode to work under cold conditions [23–30]. With decreasing temperature, the electrolyte resistance increases markedly, primarily due to elevated viscosity and decreased salt solubility. Moreover, the structure and composition of the solid electrolyte interphase (SEI) depend heavily on the electrolyte formulation and exhibit high sensitive to temperature fluctuations. It is well recognized that an electrolyte composed of sodium hexafluorophosphate ( $\text{NaPF}_6$ ) salt dissolved in diethylene glycol dimethyl ether (DEGDME) in a standard salt concentration of 1 M exhibited high compatibility with Na metal anodes, rendering it a superior choice for stable cycling at room temperature [31]. Our previous research showed that  $\text{NaPF}_6$  and sodium trifluoromethanesulfonate ( $\text{NaOTf}$ ) exhibited intermediate reduction potentials vs  $\text{Na}^+/\text{Na}$  with a moderate driving force to decompose before the decomposition of DEGDME, which may contribute to the formation of a smooth and inorganic-species-rich SEI film on the Na metal electrode at room temperature [23]. Nevertheless,  $\text{NaPF}_6$  faces solubility challenges at low temperatures; salt precipitation was observed in the 1 M  $\text{NaPF}_6$ -DEGDME electrolyte system at  $-35\text{ }^{\circ}\text{C}$ , leading to suboptimal electrochemical performance. Even at a reduced concentration of 0.5 M  $\text{NaPF}_6$ -DEGDME, a temperature



limitation of  $-40\text{ }^{\circ}\text{C}$  was still evident (Supplementary Figure S1), and similar temperature threshold was also observed with the NaOTf-DEGDME electrolyte system [23]. This phenomenon could be explained by the intrinsic molecular architecture of DEGDME. The presence of multiple oxygen atoms in DEGDME induces strong intermolecular interactions, causing sluggish diffusion of the solvated  $\text{Na}^+$  ions, especially at low temperature [29]. Moreover, the multiple oxygen coordination sites facilitate a strong chelating affinity with  $\text{Na}^+$  ions, which increases the number of solvent molecules within the solvation shell [29]. This feature is particularly detrimental for the SEI formation at low temperature, in which the salt solubility decreases and thus the decomposition of the salt is suppressed, leading to an unfavorable SEI dominated by organic species originated from the solvent molecules.

Herein we present an electrolyte formulation that replaces the widely employed DEGDME solvent for Na metal anode with monoglyme—1,2-dimethoxyethane (DME)—which enables superior performance for metallic Na anode at low temperatures down to  $-80\text{ }^{\circ}\text{C}$ . X-ray photoelectron spectroscopy (XPS) characterization on the SEI layer reveals that DME facilitates the formation of an SEI that is more enriched with inorganic species compared to that formed in DEGDME counterpart at  $-80\text{ }^{\circ}\text{C}$ . Symmetric cell testing shows that when cycled at  $-40\text{ }^{\circ}\text{C}$  at  $1\text{ mA cm}^{-2}$ , the Na metal electrode exhibits a low overpotential of only 16 mV over 750 h. Even at a high current of  $3\text{ mA cm}^{-2}$ , the overpotential is only 82 mV at  $-40\text{ }^{\circ}\text{C}$ . In addition, when cycled at an extremely cold temperature of  $-80\text{ }^{\circ}\text{C}$ , the Na metal electrode displays impressive long-term stability with a low overpotential of 54 mV sustained over 1500 h at  $0.5\text{ mA cm}^{-2}$ . Moreover, high Coulombic efficiency of 99.8% is achieved at  $-60\text{ }^{\circ}\text{C}$  for Na asymmetric cell at  $0.5\text{ mA cm}^{-2}$ . This performance is comparable to, and in many cases surpasses the reported state-of-the-art results for Na metal anodes cycling at current densities of  $\geq 0.5\text{ mA cm}^{-2}$  at ultra-low temperatures ( $\leq -40\text{ }^{\circ}\text{C}$ ), as summarized in Supplementary Table S1. Moreover, full cell evaluations when paring with  $\text{Na}_3\text{V}_2(\text{PO}_4)_3$  cathode reveal a high average Coulombic efficiency exceeding 99.1% and a capacity retention over 83% after 100 cycles at both  $-40\text{ }^{\circ}\text{C}$  and  $-80\text{ }^{\circ}\text{C}$ .

## 2. Experimental Sections

### 2.1. Chemicals and Materials

Metallic Na chips were produced from Na metal cubes obtained from Sigma–Aldrich (Shanghai Trading Co., Ltd., Shanghai, China). Prior to use, sodium hexafluorophosphate ( $\text{NaPF}_6$ , Sigma–Aldrich) was dried in an argon (Ar)-filled glove box, maintaining conditions of  $\text{O}_2 < 0.6\text{ PPM}$  and  $\text{H}_2\text{O} < 0.1\text{ PPM}$  (Mbraun). The solvents used for electrolyte preparation—diethylene glycol dimethyl ether (anhydrous, Sigma–Aldrich), 1,2-dimethoxyethane (anhydrous, Sigma–Aldrich), 1,3-dioxolane (anhydrous, Sigma–Aldrich), and tetrahydrofuran (anhydrous, Sigma–Aldrich)—were used directly without further purification.

### 2.2. Characterizations

A temperature chamber (MC-812 ESPEC Corp., Osaka, Japan) was utilized to maintain stable temperature conditions ranging from  $-80\text{ }^{\circ}\text{C}$  to  $20\text{ }^{\circ}\text{C}$ . Coin cells were equilibrated at a specified temperature for a minimum of one hour to ensure thermal stability. X-ray photoelectron spectroscopy (XPS) analysis was conducted using a PHI Versaprobe II scanning XPS microprobe (ULVAC-PHI, Inc., Kanagawa, Japan), which has a system resolution of 0.47 eV and employs a monochromatic 1486.7 eV X-ray source. Samples were transferred into the XPS chamber using a sealed Ar-filled vessel to prevent exposure to air. Differential scanning calorimetry (DSC) was performed with a Netzsch DSC 204 F1 Phoenix (NETZSCH-Gerätebau GmbH, Selb, Germany), measuring both samples and a reference between  $-150\text{ }^{\circ}\text{C}$  and  $20\text{ }^{\circ}\text{C}$  at a controlled heating rate of  $10\text{ }^{\circ}\text{C min}^{-1}$ . Additionally,  $^{23}\text{Na}$  Nuclear Magnetic Resonance (NMR) was executed on a Bruker 600 MHz Advance III HD spectrometer (Bruker Corporation, Billerica, MA, USA) equipped with a 5 mm probe (Bruker BBFO). Scanning electron microscope (SEM) imaging was carried out using a field emission gun environmental SEM (XL 300 ESEM-FEG, FEI Company, Hillsboro, OR, USA).

### 2.3. Electrochemical Measurements

All electrolytes were prepared in an argon-filled glove box. Na || Na symmetric cycling was performed in 2032-type coin cells, which consisted of two identical Na chips and a separator (Celgard 2400) saturated with  $40\text{ }\mu\text{L}$  of the testing electrolyte. Asymmetric cells were assembled with stainless steel foil as the working electrode and freshly cut Na as the counter electrode, also using  $40\text{ }\mu\text{L}$  of the electrolyte. Na metal full cells were constructed with  $\text{Na}_3\text{V}_2(\text{PO}_4)_3$  cathodes and bare Na anodes utilizing the tested electrolytes. Details regarding the synthesis and processing of  $\text{Na}_3\text{V}_2(\text{PO}_4)_3$ , as well as cathode preparation, can be found in a prior study [18]. The active material loading for the cathodes is  $2\text{ mg cm}^{-2}$ . Electrochemical evaluations of symmetric and asymmetric cells,

along with Na metal full cells, were conducted using a standard battery tester (CT2001A, Wuhan LANHE Electronics Co., Ltd., Wuhan, China). Electrochemical impedance spectroscopy (EIS) measurements were carried out using an electrochemical workstation (VMP3, Bio-Logic Science Instruments, Seyssinet-Pariset, France) over a frequency range of 1 MHz to 0.1 Hz, with an AC amplitude of 5 mV. The total resistance of the electrolyte solution was measured through EIS in stainless steel (SS) || stainless steel (SS) cells [23]. A polymer membrane was sandwiched between two pieces of stainless steel in the coin cell with 40  $\mu\text{L}$  electrolyte added. The ionic conductivity of the electrolyte solution was calculated based on the method detailed in our previous paper [23].

### 3. Results and Discussion

#### 3.1. Screening and Electrochemical Evaluation of Different Electrolytes at Low Temperatures

We first investigated a series of electrolyte solutions composed of  $\text{NaPF}_6$  salt with different solvents at  $-35\text{ }^\circ\text{C}$ . Ethers including DEGDME, DME, 1,3-dioxolane (DOL), and tetrahydrofuran (THF) were chosen as candidate solvents due to their low melting points (Supplementary Table S2). Out of the twelve formulations tested, nine exhibited good solubility with 0.5 M  $\text{NaPF}_6$  at  $-35\text{ }^\circ\text{C}$  without obvious salt precipitation (Supplementary Table S3). Based upon our previous finding that a 2:8 volume ratio of DEGDME to DOL optimized the Na metal electrode performance at  $-80\text{ }^\circ\text{C}$  [23], here we selected six representative systems (marked in Supplementary Table S3) for further systematic evaluation. To isolate the structural effects of linear ethers (DEGDME vs. DME) and cyclic ethers (DOL vs. THF), we primarily focused on the 2:8 ratio as a comparative benchmark to explore how molecular substitution—rather than concentration variance—governs low-temperature electrochemical behavior.

Repeated Na stripping and plating were performed in symmetric cells with two identical electrodes using 0.5 M  $\text{NaPF}_6$  electrolytes at a current density of  $0.2\text{ mA cm}^{-2}$  and a capacity of  $0.1\text{ mAh cm}^{-2}$  across a temperature range from  $0\text{ }^\circ\text{C}$  to  $-80\text{ }^\circ\text{C}$  (Figure 1a–c). As shown in Figure 1a, the electrolyte systems employing 0.5 M  $\text{NaPF}_6$ -DME/DOL (2:8 in volume fraction; all ratios hereafter refer to volume ratios) and 0.5 M  $\text{NaPF}_6$ -DEGDME/DOL (2:8) exhibit low overpotentials (less than 25 mV) and stable voltage profiles down to  $-80\text{ }^\circ\text{C}$ . It is noted that the cell with 0.5 M  $\text{NaPF}_6$ -DME/DOL exhibits a stabler voltage profile, especially at  $-80\text{ }^\circ\text{C}$ , compared to the one with DEGDME. A high percentage of DOL is necessary for maintaining stable voltage profiles, as the performance of the DME/DOL (5:5 and 8:2) electrolytes with higher volume ratio of DME was unsatisfactory (Figure 1b). The critical role of cyclic ether, DOL, can be mainly ascribed to the following reasons based on our prior study and previous reports [23,29,32]: (i) DOL has a much lower melting point ( $-95\text{ }^\circ\text{C}$ ) compared to DME ( $-58\text{ }^\circ\text{C}$ ), preventing the electrolyte from freezing at cold conditions and improving the ionic conductivity of the electrolyte; (ii) DOL is known as a weakly solvating solvent for  $\text{Na}^+$  and  $\text{Li}^+$  ions, which participates in the solvation shell and weakens the chelation of  $\text{Na}^+$  ions with glyme-based electrolytes; (iii) DOL may contribute to a concentrated electron cloud around  $\text{PF}_6^-$  and result in the preferential salt decomposition rather than the solvent molecules. Additionally, replacing DOL with THF in the DEGDME/THF (2:8) and DME/THF (2:8) systems resulted in asymmetric voltage profiles and high overpotentials at low temperatures, especially at ultra-low temperature of  $-60\text{ }^\circ\text{C}$  and  $-80\text{ }^\circ\text{C}$  (Figure 1c).

In addition to symmetric cells, Na || stainless steel (SS) asymmetric cells were fabricated and tested at  $0.5\text{ mA cm}^{-2}$  and  $0.5\text{ mAh cm}^{-2}$ , with a cut-off voltage of 0.3 V (Figure 1d–f) at low temperatures ranging from  $-10\text{ }^\circ\text{C}$  to  $-60\text{ }^\circ\text{C}$ . While both the DEGDME/DOL (2:8) and DME/DOL (2:8) systems exhibit comparable performance in Na || Na symmetric configurations, the 0.5 M  $\text{NaPF}_6$ -DME/DOL (2:8) system displays smoother stripping and plating curves, featuring a lower nucleation overpotential of 47 mV and a high Coulombic efficiency (CE) of 99.84% at  $-60\text{ }^\circ\text{C}$  (Figure 1d). In contrast, the 0.5 M  $\text{NaPF}_6$ -DEGDME/DOL (2:8) system has a higher nucleation overpotential of 60 mV and a much lower CE of 88.06% at  $-60\text{ }^\circ\text{C}$  (Figure 1e). In addition, the CE of the 0.5 M  $\text{NaPF}_6$ -DME/DOL (2:8) at  $-10\text{ }^\circ\text{C}$ ,  $-20\text{ }^\circ\text{C}$  and  $-40\text{ }^\circ\text{C}$  is 99.84%, 99.93% and 99.60%, respectively; these numbers are slightly higher those of the 0.5 M  $\text{NaPF}_6$ - DEGDME/DOL (2:8), which gives a CE of 99.68% at  $-10\text{ }^\circ\text{C}$ , 99.38% at  $-20\text{ }^\circ\text{C}$ , and 99.28% at  $-40\text{ }^\circ\text{C}$ . Meanwhile, the 0.5 M  $\text{NaPF}_6$ -DME/THF (2:8) system shows voltage profiles characterized by a stepwise stripping curve, with a distinct turning point at 0.15 V at  $-60\text{ }^\circ\text{C}$  (Figure 1f). This phenomenon may suggest that Na dendrite fragments, formed due to sluggish kinetics at  $-60\text{ }^\circ\text{C}$ , become partially isolated. The observed voltage step represents the stripping of this ‘inactive’ Na, which could only be recovered under increased overpotential. The CE values of the 0.5 M  $\text{NaPF}_6$ -DME/THF (2:8) at different temperatures are as follows: 99.92% at  $-10\text{ }^\circ\text{C}$ , 99.83% at  $-20\text{ }^\circ\text{C}$ , 99.84% at  $-40\text{ }^\circ\text{C}$  and 92.93% at  $-60\text{ }^\circ\text{C}$ .

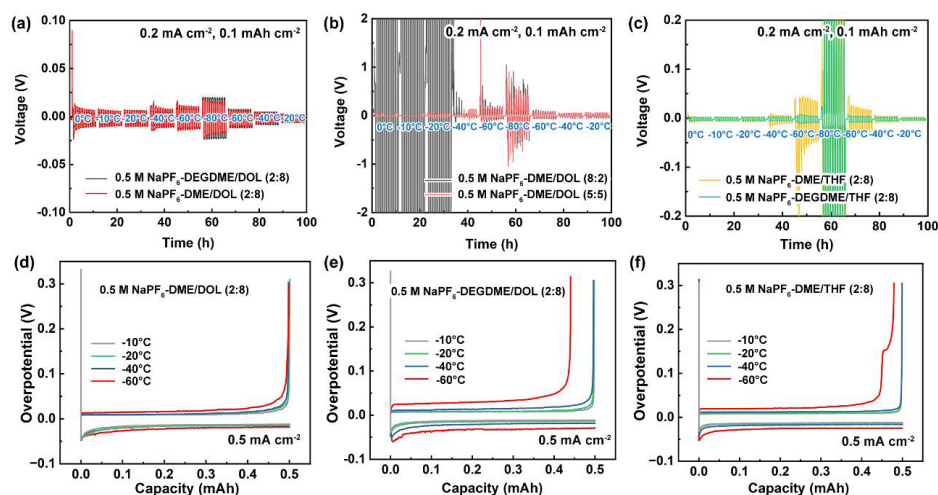


**Figure 1.** Temperature-dependent electrochemical screening of electrolyte formulations at low temperatures. Galvanostatic cycling of Na || Na symmetric cells at  $0.2 \text{ mA cm}^{-2}$  and  $0.1 \text{ mAh cm}^{-2}$  in  $0.5 \text{ M}$  electrolytes of (a)  $\text{NaPF}_6\text{-DEGDME/DOL (2:8)}$  and  $\text{NaPF}_6\text{-DME/DOL (2:8)}$ ; (b)  $\text{NaPF}_6\text{-DME/DOL (8:2)}$  and  $\text{NaPF}_6\text{-DME/DOL (5:5)}$ ; and (c)  $\text{NaPF}_6\text{-DME/THF (2:8)}$  and  $\text{NaPF}_6\text{-DEGDME/THF (2:8)}$ ; (d–f) Na plating/stripping profiles of Na || stainless steel (SS) asymmetric cells at  $0.5 \text{ mA cm}^{-2}$  and  $0.5 \text{ mAh cm}^{-2}$  with a cut-off voltage of  $0.3 \text{ V}$  in  $0.5 \text{ M}$  electrolytes of  $\text{NaPF}_6\text{-DME/DOL (2:8)}$ ,  $\text{NaPF}_6\text{-DEGDME/DOL (2:8)}$  and  $\text{NaPF}_6\text{-DME/THF (2:8)}$ .

The  $0.5 \text{ M NaPF}_6\text{-DME/DOL (2:8)}$  electrolyte was then selected for further electrochemical evaluation due to its superior performance observed during the initial screening process. This assessment focused on rate capability and long-term cycling stability in symmetric cells at  $-40 \text{ }^\circ\text{C}$  (Figure 2). In the rate capacity measurement (Figure 2a), the cell exhibits stable performance with a low overpotential of less than  $20 \text{ mV}$  with a capacity increasing from  $1 \text{ mAh cm}^{-2}$  to  $3 \text{ mAh cm}^{-2}$  at a current density of  $1 \text{ mA cm}^{-2}$ . Meanwhile, as current density was increased from  $1$  to  $2 \text{ mA cm}^{-2}$  while maintaining a constant capacity of  $1 \text{ mAh cm}^{-2}$  (Figure 2b), the overpotential of the cell rises from about  $16 \text{ mV}$  to  $48 \text{ mV}$ ; even at a high current density of  $3 \text{ mA cm}^{-2}$ , the cell only shows an overpotential of  $82 \text{ mV}$ , indicating fast kinetics at such low temperature. In addition, the  $0.5 \text{ M NaPF}_6\text{-DME/DOL (2:8)}$  electrolyte system demonstrates stable long-term cycling at  $-40 \text{ }^\circ\text{C}$ , maintaining an overpotential of approximately  $15\text{-}16 \text{ mV}$  for over  $750 \text{ h}$  at  $1 \text{ mA cm}^{-2}$  and  $1 \text{ mAh cm}^{-2}$ , without any discernible trend of increase (Figure 2c).

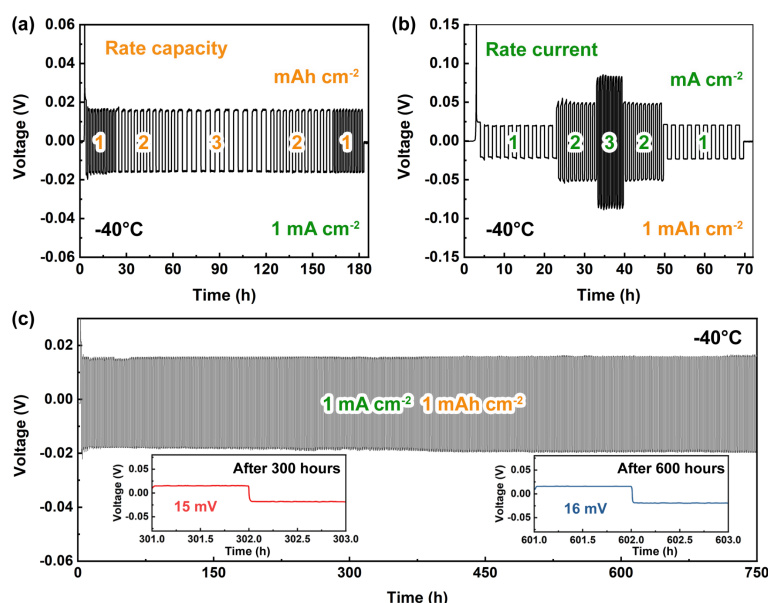


**Figure 2.** Galvanostatic cycling of Na || Na symmetric cells in  $0.5 \text{ M NaPF}_6\text{-DME/DOL (2:8)}$  electrolyte at  $-40 \text{ }^\circ\text{C}$ . (a) Rate capacity performance at various capacities up to  $3 \text{ mAh cm}^{-2}$  at  $1 \text{ mA cm}^{-2}$ ; (b) Rate current performance at various current densities up to  $3 \text{ mA cm}^{-2}$  at  $1 \text{ mAh cm}^{-2}$ ; (c) Long-term stability at  $1 \text{ mA cm}^{-2}$  and  $1 \text{ mAh cm}^{-2}$  (Insets: enlarged voltage profiles after  $300 \text{ h}$  and after  $600 \text{ h}$ ).

### 3.2. Physicochemical Characterization of the Designed Electrolyte

To investigate the interaction between  $\text{Na}^+$  ions and solvent molecules, we conducted  $^{23}\text{Na}$  nuclear magnetic resonance (NMR) spectroscopy (Figure 3a). The relative peak intensities varied with different solvent species, providing insights for the solubility characteristics of the Na species (i.e.,  $\text{NaPF}_6$ ) in the medium [33]. Notably,  $\text{NaPF}_6$  demonstrates higher solubility in DME and THF compared to DOL. The incorporation of a small fraction (20% in volume) of DME significantly enhanced salt solubility in the DME/DOL (2:8) mixture relative to pure DOL. This improved solubility was maintained even at temperatures as low as  $-80\text{ }^\circ\text{C}$  (Figure 3b). No precipitation of salt was observed for the 0.5 M  $\text{NaPF}_6$ -DME/DOL (2:8) after storing at  $-80\text{ }^\circ\text{C}$  for 24 h. Nevertheless, salt precipitation occurred in the 0.5 M  $\text{NaPF}_6$ -DME/THF (2:8) solution at  $-80\text{ }^\circ\text{C}$  (Supplementary Figure S2), despite THF having a lower melting point and a higher dielectric constant at room temperature compared to DOL (Supplementary Table S2). Additionally, the chemical shifts reveals that DME caused a more pronounced downfield shift of  $^{23}\text{Na}$  compared to DOL and THF, indicating a stronger deshielding effect on the  $^{23}\text{Na}$  nucleus [34]. Consistent with the Gutmann donor theory, this shift suggests that DME possesses a higher coordination affinity for  $\text{Na}^+$ , effectively reducing the electron density surrounding the  $\text{Na}^+$  through strong chelation.

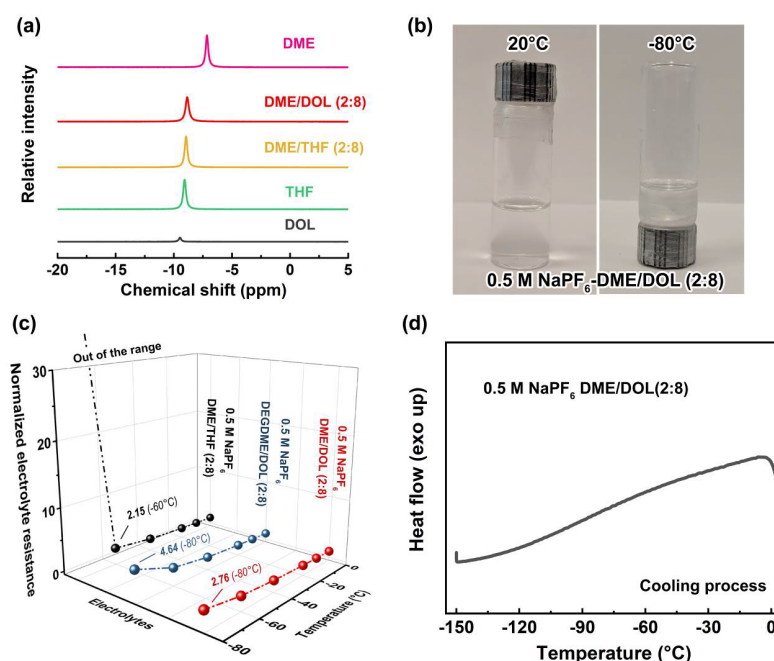


**Figure 3.** Physicochemical characterizations of  $\text{NaPF}_6$ -based electrolyte solutions. (a)  $^{23}\text{Na}$ -NMR spectroscopy on the electrolyte solutions. Notably, the concentration of the  $\text{NaPF}_6$ -DOL system is below 0.5 M due to solubility limitation, whereas the other four systems were successfully prepared at 0.5 M; (b) Photo of 0.5 M  $\text{NaPF}_6$ -DME/DOL (2:8) after storing at  $20\text{ }^\circ\text{C}$  and  $-80\text{ }^\circ\text{C}$  for 24 h. No precipitation of salts is observed at  $-80\text{ }^\circ\text{C}$ ; (c) Change in the resistance of the electrolyte solutions in the temperature range from  $0\text{ }^\circ\text{C}$  to  $-80\text{ }^\circ\text{C}$ . The resistance values at different temperatures are normalized to those at  $0\text{ }^\circ\text{C}$  (the value of each electrolyte at  $0\text{ }^\circ\text{C}$  is treated as 1). Notably, the value for the 0.5 M  $\text{NaPF}_6$ -DME/THF (2:8) at  $-80\text{ }^\circ\text{C}$  exceeds the plotted scale, shown as ‘out of the range’ in the figure; (d) DSC thermograms of 0.5 M  $\text{NaPF}_6$ -DME/DOL (2:8) electrolyte from  $0\text{ }^\circ\text{C}$  to  $-150\text{ }^\circ\text{C}$ .

To elucidate the underlying mechanism for the enhanced performance, we examined the electrolyte resistance at various temperatures (Figure 3c). Electrochemical impedance spectroscopy (EIS) was used to measure the resistance of the electrolyte solution in SS || SS cells (see Experimental Sections for details). The resistance of 0.5 M  $\text{NaPF}_6$ -DME/DOL (2:8) was approximately 6.3 Ohms at  $0\text{ }^\circ\text{C}$ , which increased by a factor of 2.76 when the temperature decreased to  $-80\text{ }^\circ\text{C}$ . This increase is half that observed for 0.5 M  $\text{NaPF}_6$ -DEGDME/DOL (2:8), which showed a 4.64-fold increase from  $0\text{ }^\circ\text{C}$  to  $-80\text{ }^\circ\text{C}$ . In contrast, the resistance of the DME/THF (2:8) system increased by a factor of 2.15 when the temperature decreased to  $-60\text{ }^\circ\text{C}$  and exceeded 30 times at  $-80\text{ }^\circ\text{C}$  due to salt precipitation. Furthermore, the observed changes in electrolyte resistance correlate well with the trends in ionic conductivity (Supplementary Figure S3), where the 0.5 M  $\text{NaPF}_6$ -DME/DOL (2:8) system exhibits the slowest decline in conductivity with decreasing temperature. Differential scanning calorimetry (DSC) further confirmed the thermal stability of the 0.5 M  $\text{NaPF}_6$ -DME/DOL (2:8) system, indicating no phase transitions even down to  $-150\text{ }^\circ\text{C}$  (Figure 3d).

### 3.3. Electrochemical Behavior at $-80\text{ }^{\circ}\text{C}$ and Post-Mortem Analysis

Extended cycling of Na || Na symmetric cells was performed utilizing 0.5 M NaPF<sub>6</sub>-DME/DOL (2:8) at  $-80\text{ }^{\circ}\text{C}$  at different current densities and capacities. At a current density of  $0.2\text{ mA cm}^{-2}$  with a cycling capacity of  $0.1\text{ mAh cm}^{-2}$ , the cell exhibits a low overpotential of approximately 20 mV, remaining stable for over 2000 h (Supplementary Figure S4). Furthermore, at a higher current density of  $0.5\text{ mA cm}^{-2}$  with a capacity of  $0.25\text{ mAh cm}^{-2}$ , stable performance was maintained for more than 1500 h (Figure 4a). The expanded voltage profiles (insets in Figure 4a) after 750 and 1500 h show smooth voltage responses without spikes with an overpotential of 53 mV and 54 mV, respectively. Scanning electron microscopy (SEM) imaging of the Na metal electrode after 50 cycles at  $-80\text{ }^{\circ}\text{C}$  reveals a uniform morphology in the NaPF<sub>6</sub>-DME/DOL (2:8) system, with no obvious porous structures on the surface or within the cross-section (Figure 4b). In contrast, the Na metal surface cycled with NaPF<sub>6</sub>-DEGDME/DOL (2:8) exhibits rough and heterogeneous textures (Supplementary Figure S5).

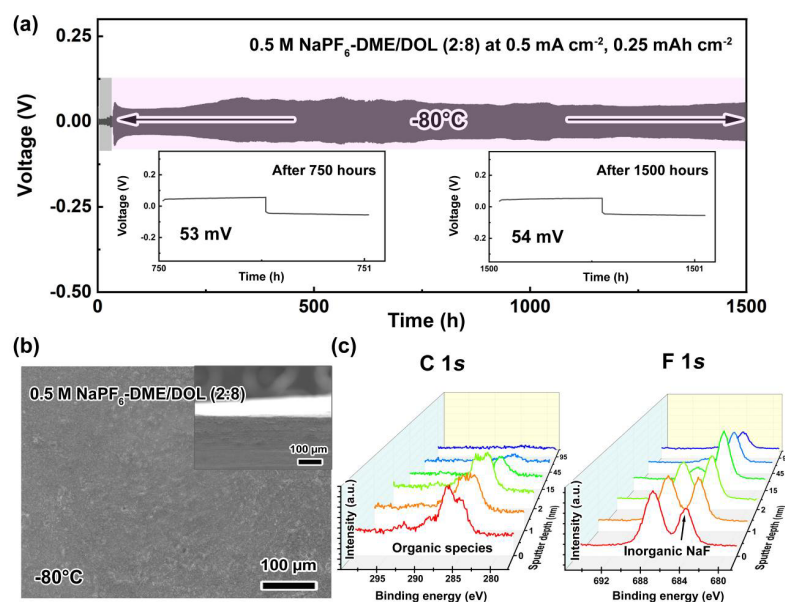


**Figure 4.** Electrochemical and physicochemical characterizations of Na metal electrodes cycled in 0.5 M NaPF<sub>6</sub>-DME/DOL (2:8) electrolyte at  $-80\text{ }^{\circ}\text{C}$ . **(a)** Galvanostatic cycling of Na || Na symmetric cells at  $0.5\text{ mA cm}^{-2}$  and  $0.25\text{ mAh cm}^{-2}$  (pink zone). Note that an initial stepwise temperature drop (gray zone) was applied to stabilize the cells (Insets: enlarged voltage profiles after 750 h and after 1500 h); **(b)** Ex situ postmortem SEM imaging of the surface of the Na metal electrode after cycling at  $-80\text{ }^{\circ}\text{C}$  (Inset: corresponding cross-sectional SEM image); **(c)** XPS profiles of the C 1s and F 1s spectra recorded at various sputtering depths.

The chemical composition of the Na metal electrode surface using 0.5 M NaPF<sub>6</sub>-DME/DOL (2:8) was characterized using X-ray photoelectron spectroscopy (XPS), as illustrated in Supplementary Figure S6. Binding energies for all elements were calibrated relative to the C 1s signal at 284.8 eV. In the C 1s spectrum, the peak at 293 eV corresponds to polycarbonate, and the peaks at 289.5 eV and 286.8 eV can be attributed to O=C=O/CO<sub>3</sub><sup>2-</sup> and C–O, respectively [19,31,33,35,36]. For the O 1s spectrum, the peaks at 532.5 eV and 526 eV can be assigned to O–P=O and Na<sub>2</sub>O [19], respectively, while the peak at 537 eV is associated with Na KLL [19,35]. With respect to the F 1s spectrum, the peaks at 687.6 eV and 684.2 eV correspond to PF<sub>6</sub><sup>-</sup> and NaF species, respectively [19,35]. The P 2p spectrum shows doublets at 137.4 eV and 133.7 eV (for 2p<sub>3/2</sub>), which are assigned to PF<sub>6</sub><sup>-</sup> and O–P=O. The signal of O–P=O is potentially originated from Na<sub>x</sub>PF<sub>y</sub>O<sub>z</sub>, a major decomposition product of NaPF<sub>6</sub> [19]. The XPS results indicate a major composition of organic and inorganic species (mainly including NaF and Na<sub>2</sub>O) on the Na metal electrode surface. Detailed identification of the XPS peaks is provided in Supplementary Table S4.

To further investigate the distribution of chemical species within the SEI formed with NaPF<sub>6</sub>-DME/DOL (2:8), XPS depth profiling was conducted (Figure 4c and Supplementary Figures S6 and S7). The signal for the carbon content decreases with increasing depth and completely vanishes at around 95 nm beneath the surface, revealing that the organic debris predominantly resides in the upper layer of the SEI. This also indicates that the thickness of the SEI is approximately 95 nm. Moreover, the NaF content increases with depth till reaching around 15 nm, suggesting a higher percentage of NaF existing in the inner region of the SEI (Figure 4c). The NaF signal was still detectable while the signal of the carbon content disappeared, suggesting that the NaPF<sub>6</sub> salt decomposed

before the decomposition of the solvent molecules. For comparison, XPS characterization was also performed on the surface of the Na metal electrode using 0.5 M NaPF<sub>6</sub>-DEGDME/DOL (2:8) at −80 °C (Supplementary Figure S8). It shows that the surface of the SEI contains much fewer inorganic species, especially NaF, in contrast to the SEI formed in the 0.5 M NaPF<sub>6</sub>-DME/DOL (2:8), indicating that NaF is critical in maintaining the integrity of the SEI over cycling. Meanwhile, the signal of the O-P=O, which is associated with the NaPF<sub>6</sub> decomposition, is weaker in the SEI formed in the DEGDME system compared with that formed in the DME system. The XPS analyses revealed that the DME/DOL electrolyte system, in contrast to the commonly utilized DEGDME/DOL system, can facilitate the decomposition of the NaPF<sub>6</sub> salt at low operating temperatures. This could be attributed to the weaker binding affinity of the DME molecule for Na<sup>+</sup> ions, resulting from its fewer oxygen coordination sites than DEGDME; this reduces the number of solvent molecules within the solvation shell and subsequently promotes the salt decomposition [29].

### 3.4. Electrochemical Performance of Full Na Metal Cells at Low Temperatures

To evaluate the full cell performance of the formulated electrolyte of 0.5 M NaPF<sub>6</sub>-DME/DOL (2:8), Na metal batteries utilizing Na<sub>3</sub>V<sub>2</sub>(PO<sub>4</sub>)<sub>3</sub> as the cathode and Na metal as the anode were assembled and tested under a series of low temperatures ranging from −10 °C down to −80 °C (Figure 5). The charge–discharge voltage profiles at 0.2C (1C = 110 mA g<sup>−1</sup>) (Figure 5a) reveal that both voltage hysteresis and capacity utilization are highly sensitive to the operating temperature. At a relatively mild low temperature of −10 °C, the cell delivers a specific capacity of ~100 mA g<sup>−1</sup>, representing 91% of its theoretical capacity. As the temperature decreases, the discharge voltage plateaus become progressively shorter and shift to lower potentials due to increased internal resistance and sluggish diffusion kinetics. Notably, the cell still maintains great capacity retention at −40 °C and −60 °C, delivering 72% and 45% of its theoretical capacity, respectively. The detectable performance even at −80 °C highlights the exceptional low-temperature resilience of this system. The rate performance of the cells at −40 °C is illustrated in Figure 5b, demonstrating the viability of Na metal cycling in a full cell configuration using the formulated electrolyte under cold conditions. As the discharge current increases up to 1C, the specific discharge capacity decreases, with approximately 79% of the capacity achieved at 0.2C retained at 1C. It is noted that this capacity loss is reversible, with full recovery observed upon reverting the current rate to 0.2C (Figure 5b). For long-term cycling performance at −40 °C (Figure 5c), the battery exhibits an initial discharge capacity of 86.3 mAh g<sup>−1</sup>, and 86% of this capacity was maintained after 100 cycles, accompanied by an average CE of 99.1%. At −80 °C, the system maintains a high CE of 99.3% with 83% capacity retention after 100 cycles.

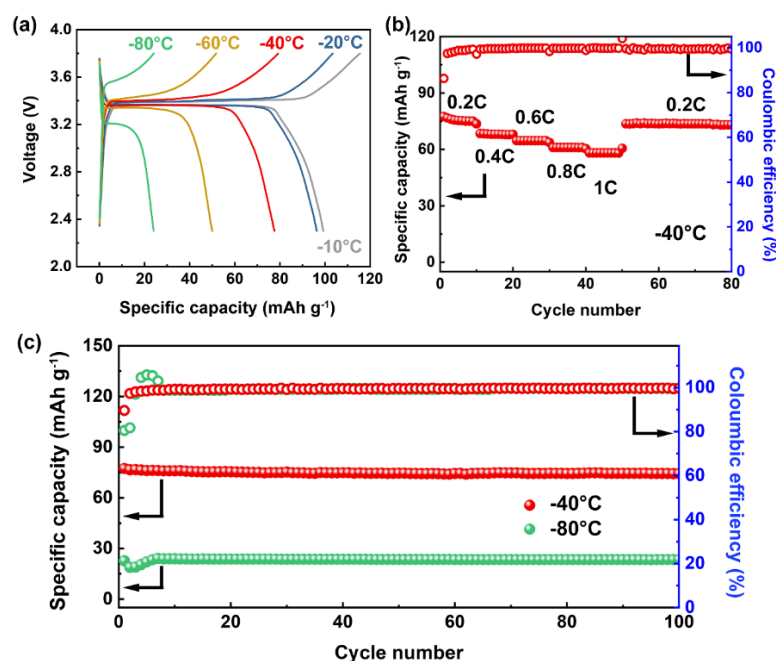


**Figure 5.** Electrochemical performance of Na || Na<sub>3</sub>V<sub>2</sub>(PO<sub>4</sub>)<sub>3</sub> cells using the 0.5 M NaPF<sub>6</sub>-DME/DOL (2:8) electrolyte at low temperatures. (a) Galvanostatic charge-discharge voltage profiles at 0.2C (1C=110 mA g<sup>−1</sup>, based on the active material of Na<sub>3</sub>V<sub>2</sub>(PO<sub>4</sub>)<sub>3</sub>) from −10 °C to −80 °C; (b) Rate performance of cells up to 1C with voltage cutoffs of 2.3 and 3.8 V at −40 °C. c, Long-term galvanostatic cycling of cells at 0.2C at −40 °C and −80 °C.

## 4. Conclusions

In summary, we demonstrated that the monoglyme, DME, would be a better solvent option compared to the conventional DEGDME to formulate an electrolyte for Na metal electrode to work under extremely cold conditions. The optimized electrolyte formulation of 0.5 M NaPF<sub>6</sub>-DME/DOL (2:8) enables stable cycling of Na metal down to  $-40\text{ }^{\circ}\text{C}$ , exhibiting a low overpotential of 16 mV at  $1\text{ mA cm}^{-2}$  with a capacity of  $1\text{ mAh cm}^{-2}$  sustained for over 750 h. This low overpotential can be maintained even at a capacity of  $3\text{ mAh cm}^{-2}$  ( $1\text{ mA cm}^{-2}$ ), while a slightly elevated overpotential of 82 mV is observed at a higher current density of  $3\text{ mA cm}^{-2}$  ( $1\text{ mAh cm}^{-2}$ ). Furthermore, stable Na cycling at  $-80\text{ }^{\circ}\text{C}$  is achieved with a small overpotential of 54 mV for over 1500 h at  $0.5\text{ mA cm}^{-2}$ . The superior performance is attributed to a relatively modest increase in the electrolyte resistance, which rises by only 2.76 times from  $0\text{ }^{\circ}\text{C}$  to  $-80\text{ }^{\circ}\text{C}$ . Additionally, the formation of a robust, NaF-rich SEI with a uniform morphology—characterized by SEM and XPS—contributes significantly to the observed electrochemical performance. As a proof of concept, Na metal batteries featuring Na<sub>3</sub>V<sub>2</sub>(PO<sub>4</sub>)<sub>3</sub> as the cathode and Na metal as the anode exhibit stable cycling and high CE values during operation down to  $-80\text{ }^{\circ}\text{C}$ .

**Supplementary Materials:** The following supporting information can be downloaded at: <https://media.sciltp.com/articles/others/2603311457275841/MI-26030022-SM.pdf>. Figure S1: Galvanostatic cycling of Na || Na symmetric cells at  $0.2\text{ mA cm}^{-2}$  and  $0.1\text{ mAh cm}^{-2}$  in an electrolyte composed of 0.5 M NaPF<sub>6</sub>-DEGDME. Figure S2: Photos of 0.5 M NaPF<sub>6</sub>-DME/THF (2:8) after storing at  $20\text{ }^{\circ}\text{C}$  and  $-80\text{ }^{\circ}\text{C}$  for 24 h (Salt precipitation was observed at the bottom of the vial at  $-80\text{ }^{\circ}\text{C}$ ). Figure S3: Temperature dependent ionic conductivity of 0.5 M NaPF<sub>6</sub>-DME/THF (2:8), 0.5 M NaPF<sub>6</sub>-DEGDME/DOL (2:8) and 0.5 M NaPF<sub>6</sub>-DME/DOL (2:8). Figure S4: Galvanostatic cycling of Na || Na symmetric cells at  $0.2\text{ mA cm}^{-2}$  and  $0.1\text{ mAh cm}^{-2}$  at  $-80\text{ }^{\circ}\text{C}$ . Note that initial stepwise temperature drop was carried out to stabilize the cells. Figure S5: SEM image of Na metal surface after 50 cycles in 0.5 M NaPF<sub>6</sub>-DEGDME/DOL (2:8) at  $-80\text{ }^{\circ}\text{C}$  (Inset: corresponding cross-sectional SEM image). Figure S6: XPS depth profile analysis on the Na metal electrode after 50 cycles (symmetric Na || Na cells) at a current density of  $0.5\text{ mA cm}^{-2}$  with a capacity of  $0.5\text{ mAh cm}^{-2}$  in 0.5 M NaPF<sub>6</sub>-DME/DOL (2:8) electrolyte at  $-80\text{ }^{\circ}\text{C}$ . Figure S7: Contents of elements determined by ex-situ postmortem XPS depth profiling of the Na metal electrode (symmetric Na || Na cells) in 0.5 M NaPF<sub>6</sub>-DME/DOL (2:8) after cycling at  $-80\text{ }^{\circ}\text{C}$ . Figure S8: XPS profiles of C 1s, O 1s, F 1s and P 2p of the Na metal surface after 50 cycles (symmetric Na || Na cells) in 0.5 M NaPF<sub>6</sub>-DEGDME/DOL (2:8) at  $0.5\text{ mA cm}^{-2}$  and  $0.5\text{ mAh cm}^{-2}$  at  $-80\text{ }^{\circ}\text{C}$ . Table S1: Summary comparing performance of Na metal anodes (symmetric cells of Na/Na) cycling at current density  $\geq 0.5\text{ mA cm}^{-2}$  and at low temperatures ( $\leq 40\text{ }^{\circ}\text{C}$ ). Table S2: Melting point, dielectric constant, and dynamic viscosity of DEGDME, DME, DOL and THF [1–3,6]. Table S3: Summary of NaPF<sub>6</sub> salt dissolution in binary solvents at 0.5 M concentrations at  $-35\text{ }^{\circ}\text{C}$  (“Yes” indicates fully dissolved; “No” indicates not fully dissolved; “Partially” indicates slight solid precipitation as the electrolyte approached its saturation point; “\*” indicates the six electrolytes systems that were selected for the further electrochemical evaluation). Table S4: Summary of identified XPS peaks [7–11]. References [37] are cited in supplementary materials.

**Author Contributions:** C.W. and W.L.: conceived the idea; C.W.: conducted the electrolyte formulation and material characterization; C.W. and P.W.: performed electrochemical evaluation; C.W., P.W. and W.L.: cowrote the paper. All the authors discussed the results and commented on the manuscript

**Funding:** This work was funded by the U.S. Department of Energy, Office of Science, Basic Energy Sciences, under Award #DE-SC002624.

**Data Availability Statement:** Data are available from the corresponding author upon reasonable request.

**Conflicts of Interest:** The authors declare no conflict of interest.

**Use of AI and AI-Assisted Technologies:** No AI tools were used to prepare this paper.

## References

1. Dunn, B.; Kamath, H.; Tarascon, J.-M. Electrical energy storage for the grid: A battery of choices. *Science* **2011**, *334*, 928–935.
2. Goodenough, J.; Park, K.-S. The Li-ion rechargeable battery: A perspective. *J. Am. Chem. Soc.* **2013**, *135*, 1167–1176.
3. Tarascon, J.-M.; Armand, M. Issues and challenges facing rechargeable lithium batteries. *Nature* **2001**, *414*, 359–367.
4. Zhang, S.; Xu, K.; Jow, T. The low temperature performance of Li-ion batteries. *J. Power Sources* **2003**, *115*, 137–140.
5. Xu, J.; Wang, X.; Yuan, N.; Ding, J.; Qin, S.; Razal, J.; Wang, X.; Ge, S.; Gogotsi, Y. Extending the low temperature operational limit of Li-ion battery to  $-80\text{ }^{\circ}\text{C}$ . *Energy Storage Mater.* **2019**, *23*, 383–389.
6. Zhu, G. Materials insights into low-temperature performances of lithium-ion batteries. *J. Power Sources* **2015**, *300*, 29–40.
7. Yoon, S.; Cavallaro, K.; Park, B.; Yook, H.; Han, J.; McDowell, M. Controlling solvation and solid-electrolyte interphase formation to enhance lithium interfacial kinetics at low temperatures. *Adv. Funct. Mater.* **2023**, *38*, 2302778.
8. Gupta, A.; Manthiram, A. Designing advanced lithium-based batteries for low-temperature conditions. *Adv. Energy Mater.* **2020**, *10*, 2001972.
9. Dong, X.; Lin, Y.; Li, P.; Ma, Y.; Huang, J.; Bin, D.; Wang, Y.; Qi, Y.; Xia, Y. High-energy rechargeable metallic lithium battery at  $-70\text{ }^{\circ}\text{C}$  enabled by a cosolvent electrolyte. *Angew. Chem. Int. Ed.* **2019**, *58*, 5623–5627.

10. Thenuwara, A.; Shetty, P.; Kondekar, N.; Sandoval, S.; Cavallaro, K.; May, R.; Yang, C.; Marbella, L.; Qi, Y.; McDowell, M. Efficient low-temperature cycling of lithium metal anodes by tailoring the solid-electrolyte interphase. *ACS Energy Lett.* **2020**, *5*, 2411–2420.
11. Holoubek, J.; Kim, K.; Yin, Y.; Wu, Z.; Liu, H.; Li, M.; Chen, A.; Gao, H.; Cai, G.; Pascal, T. et al. Electrolyte design implications of ion-pairing in low-temperature Li metal batteries. *Energy Environ. Sci.* **2022**, *15*, 1647–1658.
12. Tan, S.; Shadike, Z.; Cai, X.; Lin, R.; Kludze, A.; Borodin, O.; Lucht, B.; Wang, C.; Hu, E.; Xu, K.; et al. Review on low-temperature electrolytes for lithium-ion and lithium metal batteries. *Electrochem. Energy Rev.* **2023**, *6*, 35.
13. Weng, S.; Zhang, X.; Yang, G.; Zhang, S.; Ma, B.; Liu, Q.; Liu, Y.; Peng, C.; Chen, H.; Yu, H. et al. Temperature-dependent interphase formation and Li<sup>+</sup> transport in lithium metal batteries. *Nat Commun* **2023**, *14*, 4474.
14. Zhang, W.; Lu, Y.; Feng, Q.; Wang, H.; Cheng, G.; Liu, H.; Cao, Q.; Luo, Z.; Zhou, P.; Xia, Y. et al. Multifunctional electrolyte additive for high power lithium metal batteries at ultra-low temperatures. *Nat Commun* **2025**, *16*, 3344.
15. Peng, Z.; Ding, K.; Lai, M.; Qiu, R.; Xiao, Y.; Shi, J.; Guan, X.; Cai, Y.; Xu, C.; Wang, F.; et al. Rational electrolyte solvent screening for high-energy lithium metal batteries at low temperatures. *Nat Commun* **2026**, *17*, 590.
16. Holoubek, J.; Liu, H.; Wu, Z.; Yin, Y.; Xing, X.; Cai, G.; Yu, S.; Zhou, H.; Pascal, T.; Chen, Z.; et al. Tailoring electrolyte solvation for Li metal batteries cycled at ultra-low temperature. *Nat Energy* **2021**, *6*, 303–313.
17. Wang, H.; Wang, C.; Matios, E.; Li, W. Critical role of ultrathin graphene films with tunable thickness in enabling highly stable sodium metal anodes. *Nano Lett.* **2017**, *17*, 6808–6815.
18. Wang, C.; Wang, H.; Matios, E.; Hu, X.; Li, W. A chemically engineered porous copper matrix with cylindrical core-shell skeleton as a stable host for metallic sodium anodes. *Adv. Funct. Mater.* **2018**, *28*, 1802282.
19. Wang, H.; Wang, C.; Matios, E.; Li, W. Facile stabilization of the sodium metal anode with additives: Unexpected key role of sodium polysulfide and adverse effect of sodium nitrate. *Angew. Chem. Int. Ed.* **2018**, *57*, 7734–7737.
20. Wang, H.; Matios, E.; Luo, J.; Li, W. Combining theories and experiments to understand the sodium nucleation behavior towards safe sodium metal batteries. *Chem. Soc. Rev.* **2020**, *49*, 3783–3805.
21. Zhao, Y.; Adair, K.; Sun, X. Recent developments and insights into the understanding of Na metal anodes for Na-metal batteries. *Energy Environ. Sci.* **2018**, *11*, 2673–2695.
22. Lee, B.; Paek, E.; Mitlin, D.; Lee, S. Sodium Metal Anodes: Emerging Solutions to Dendrite Growth. *Chem. Rev.* **2019**, *119*, 8, 5416–5460.
23. Wang, C.; Thenuwara, A.C.; Luo, J.; Shetty, P.; McDowell, M.; Zhu, H.; Posada-Pérez, S.; Xiong, H.; Hautier, G.; Li, W. Extending the low-temperature operation of sodium metal batteries combining linear and cyclic ether-based electrolyte solutions. *Nat Commun.* **2022**, *13*, 4934.
24. Thenuwara, A.C.; Shetty, P.; Kondekar, N.; Wang, C.; Li, W.; McDowell, M. Enabling highly reversible sodium metal cycling across a wide temperature range with dual-salt electrolytes. *J. Mater. Chem. A* **2021**, *9*, 10992–11000.
25. Cheng, F.; Hu, J.; Zhang, W.; Guo, B.; Yu, P.; Sun, X.; Peng, J. Reviving ether-based electrolytes for sodium-ion batteries. *Energy Environ. Sci.* **2025**, *18*, 6874–6898.
26. Ge, B.; Deng, J.; Wang, Z.; Liang, Q.; Hu, L.; Ren, X.; Li, R.; Lin, Y.; Li, Y.; Wang, Q. et al. Aggregate-Dominated Dilute Electrolytes with Low-Temperature-Resistant Ion-Conducting Channels for Highly Reversible Na Plating/Stripping. *Adv. Mater.* **2024**, *36*, 2408161.
27. Hu, X.; Matios, E.; Zhang, Y.; Wang, C.; Luo, J.; Li, W. Deeply cycled sodium metal anodes at low temperature and in lean electrolyte conditions. *Angew. Chem. Int. Ed.* **2021**, *60*, 5978–5983.
28. Zhou, J.; Wang, Y.; Wang, J.; Liu, Y.; Li, Y.; Chen, L.; Ding, D.; Dong, S.; Zhu, Q.; Tang, M. et al. Low-temperature and high-rate sodium metal batteries enabled by electrolyte chemistry. *Energy Storage Mater.* **2022**, *50*, 47–54.
29. Hu, L.; Deng, J.; Lin, Y.; Liang, Q.; Ge, B.; Weng, Q.; Bai, Y.; Li, Y.; Deng, Y.; Chen, G.; et al. Restructuring electrolyte solvation by a versatile diluent toward beyond 99.9% coulombic efficiency of sodium plating/stripping at ultralow temperatures. *Adv. Mater.* **2024**, *36*, 2312161.
30. Zhu, Q.; Yu, D.; Chen, J.; Cheng, L.; Tang, M.; Wang, Y.; Li, Y.; Yang, J.; Wang, H. A 110 Wh kg<sup>-1</sup> Ah-level anode-free sodium battery at -40 °C. *Joule* **2024**, *8*, 482–495.
31. Seh, Z.; Sun, J.; Sun, Y.; Cui, Y. A highly reversible room-temperature sodium metal anode. *ACS Cent. Sci.* **2015**, *1*, 449–455.
32. Cui, Y.; Ni, Y.; Wang, Y.; Wang, L.; Yang, W.; Wu, S.; Xie, W.; Zhang, K.; Yan, Z.; Chen, J. A temperature-adapted ultraweakly solvating electrolyte for cold-resistant sodium-ion batteries. *Adv. Energy Mater.* **2025**, *15*, 2405363.
33. Lutz, L.; Cortz, D.; Tang, M.; Salager, E.; Deschamps, M.; Grimaud, A.; Johnson, L.; Bruce, P.; Tarascon, J. Role of electrolyte anions in the Na–O<sub>2</sub> battery: Implications for NaO<sub>2</sub> solvation and the stability of the sodium solid electrolyte interphase in glyme ethers. *Chem. Mater.* **2017**, *29*, 6066–6075.
34. Cresce, A.; Russell, S.; Borodin, O.; Allen, J.; Schroeder, M.; Dai, M.; Peng, J.; Gobet, M.; Greenbaum, S.; Rogers, R.; et al. Solvation behavior of carbonate-based electrolytes in sodium ion batteries. *Phys. Chem. Chem. Phys.* **2017**, *19*, 574–586.

35. Moulder, J.F. *Handbook of X-ray Photoelectron Spectroscopy: A Reference Book of Standard Spectra for Identification and Interpretation of XPS Data*; Physical Electronics Division, Perkin-Elmer Corporation Press: Eden Prairie, MI, USA, 1992.
36. Fiedler, C.; Luerssen, B.; Rohnke, M.; Sann, J.; Janek, J. XPS and SIMS analysis of solid electrolyte interphases on lithium formed by ether-based electrolytes. *J. Electrochem. Soc.* **2017**, *164*, A3742–A3749.
37. Aminabhavi, T.; Gopalakrishna, B. Density, viscosity, refractive index, and speed of sound in aqueous mixtures of N,N-dimethylformamide, dimethyl sulfoxide, N,N-dimethylacetamide, acetonitrile, ethylene glycol, diethylene glycol, 1,4-dioxane, tetrahydrofuran, 2-methoxyethanol, and 2-ethoxyethanol at 298.15 K. *J. Chem. Eng. Data* **1995**, *40*, 856–861.